

Vertical Structure of the Beaufort Gyre Halocline and the Crucial Role of the Depth-Dependent Eddy Diffusivity

JESSICA S. KENIGSON,^{a,d} RENSKÉ GELDERLOOS,^b AND GEORGY E. MANUCHARYAN^c

^a *Department of Earth and Planetary Sciences, Yale University, New Haven, Connecticut*

^b *Department of Earth and Planetary Sciences, The Johns Hopkins University, Baltimore, Maryland*

^c *School of Oceanography, University of Washington, Seattle, Washington*

(Manuscript received 12 April 2020, in final form 14 December 2020)

ABSTRACT: Theories of the Beaufort Gyre (BG) dynamics commonly represent the halocline as a single layer with a thickness depending on the Eulerian-mean and eddy-induced overturning. However, observations suggest that the isopycnal slope increases with depth, and a theory to explain this profile remains outstanding. Here we develop a multilayer model of the BG, including the Eulerian-mean velocity, mesoscale eddy activity, diapycnal mixing, and lateral boundary fluxes, and use it to investigate the dynamics within the Pacific Winter Water (PWW) layer. Using theoretical considerations, observational data, and idealized simulations, we demonstrate that the eddy overturning is critical in explaining the observed vertical structure. In the absence of the eddy overturning, the Ekman pumping and the relatively weak vertical mixing would displace isopycnals in a nearly parallel fashion, contrary to observations. This study finds that the observed increase of the isopycnal slope with depth in the climatological state of the gyre is consistent with a Gent–McWilliams eddy diffusivity coefficient that decreases by at least 10%–40% over the PWW layer. We further show that the depth-dependent eddy diffusivity profile can explain the relative magnitude of the correlated isopycnal depth and layer thickness fluctuations on interannual time scales. Our inference that the eddy overturning generates the isopycnal layer thickness gradients is consistent with the parameterization of eddies via a Gent–McWilliams scheme but not potential vorticity diffusion. This study implies that using a depth-independent eddy diffusivity, as is commonly done in low-resolution ocean models, may contribute to misrepresentation of the interior BG dynamics.

KEYWORDS: Arctic; Eddies; Ocean dynamics

1. Introduction

a. The Beaufort Gyre circulation

The Beaufort Gyre in the Canadian Basin of the Arctic Ocean is driven by the anticyclonic winds associated with the Beaufort High sea level pressure center (Proshutinsky and Johnson 1997). Ekman convergence accumulates low-salinity water (e.g., from river discharge and sea ice loss) and deforms the isopycnals, inducing an anticyclonic circulation in the halocline (Fig. 1a; Proshutinsky et al. 2002). The Beaufort Gyre contains $\sim 20\,000\text{ km}^3$ of freshwater, about one-fifth of the Arctic Ocean's total (Haine et al. 2015). When the atmospheric forcing relaxes (i.e., is anomalously cyclonic) for a sustained period, freshwater is thought to be released from storage and fluxed to the subarctic seas. The weakening of the Beaufort Gyre in an ocean–sea ice model has been found to coincide with the so-called “Great Salinity Anomaly” events of the 1970s–90s (Proshutinsky et al. 2015), in which freshwater pulses circulated through the North Atlantic subpolar gyre (Dickson et al. 1988; Belkin et al. 1998; Belkin 2004). Upper-ocean freshening inhibits deep convective mixing in the Labrador Sea and Nordic seas, a process by which air–sea heat

fluxes remove sufficient buoyancy to destabilize the stratification (Gelderloos et al. 2012; Lauvset et al. 2018). Therefore, Beaufort Gyre dynamics have potentially important implications for the thermohaline circulation (Jackson and Vellinga 2013), which has far-reaching connections with the broader climate system through its role in transporting surface heat and carbon to depth (Buckley and Marshall 2016).

The Beaufort Gyre undergoes significant interannual variability. Recently, anomalously anticyclonic conditions have prevailed, as indicated by the deepening of isopycnals in the halocline (Zhong et al. 2019) and the accumulation of $\sim 500\text{ km}^3\text{ yr}^{-1}$ of freshwater during 2003–18 (Proshutinsky et al. 2019a,b). The volume of Pacific Winter Water (PWW) (i.e., the water mass bounded by the 1026–1027 kg m^{-3} isopycnals between ~ 100 – 200 -m depth) alone increased by 5000 km^3 , or about 18%, during 2002–16 (Zhong et al. 2019). The significant loss of sea ice after 2007 and the coincident spinup of the gyre have resulted in enhanced mechanical energy input because of a combined impact from wind and ice stresses (Armitage et al. 2020). Understanding the key processes leading to these changes and predicting the overall evolution of the Beaufort Gyre remains a major challenge.

Among the factors that have been hypothesized to affect the halocline dynamics are the Ekman pumping, sea ice cover, mesoscale eddies, and diabatic mixing. Observations indicate that Ekman pumping, driven by both sea ice and wind-induced ocean stresses, plays a major role in the halocline deepening (Proshutinsky et al. 2019b; Meneghello et al. 2018a,b, 2020). However, observations also suggest that the halocline is

^d Current affiliation: Department of Applied Mathematics, University of Colorado Boulder, Boulder, Colorado.

Corresponding author: J. S. Kenigson, jessica.kenigson@colorado.edu

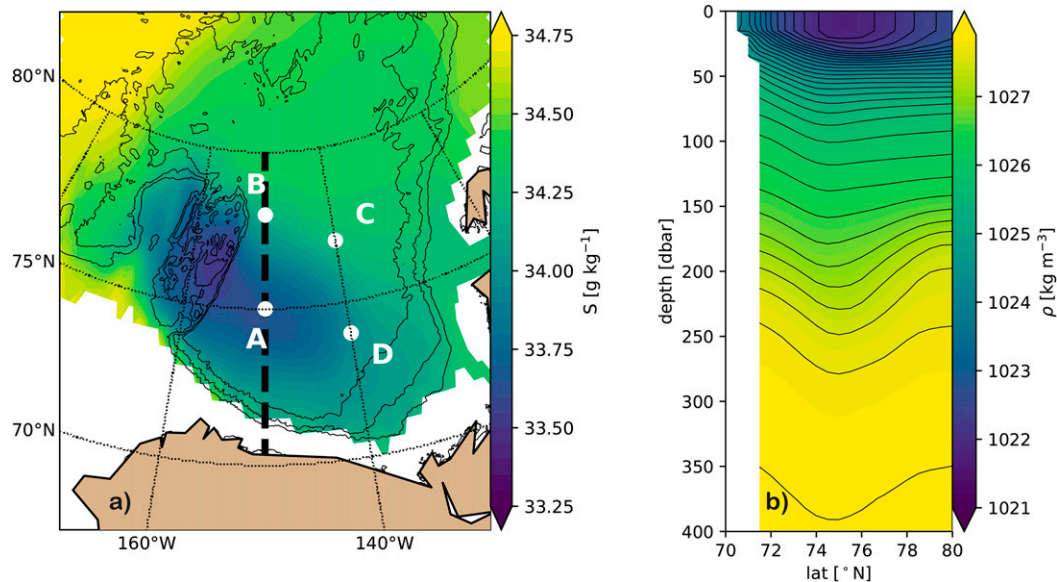


FIG. 1. (a) Annual-mean salinity from the MIMOC (Schmidtko et al. 2013) at 200 dbar showing the pronounced salinity minimum in the Beaufort Gyre (color map). Bathymetry contours are shown in intervals of 1000 m (solid black lines). The dashed black line is the location of the pressure–latitude transect at 150°W shown in (b). White dots are the locations of BGOS moorings A–D. (b) Latitude–pressure transect at 150°W, showing the annual mean potential density (referenced to 0 dbar) as calculated from the MIMOC temperature and salinity data using the TEOS-10 equations of state. Selected isopycnals are indicated by black lines.

baroclinically unstable as mesoscale eddies are ubiquitous in the Canada Basin (Zhao et al. 2016, 2018). In general, mesoscale eddies can redistribute isopycnal layer thicknesses laterally and as a result affect the halocline depth (Manucharyan and Spall 2016). In addition, on sufficiently long time scales the vertical mixing can lead to significant changes in the halocline structure (Spall 2013). At present, the basic dynamical balance of the Beaufort Gyre remains uncertain and multiple theories have been proposed that can be at odds with one another and with the observational evidence in certain respects. Below we summarize existing Beaufort Gyre models and discuss their limitations with respect to capturing these dynamics.

b. Theories of the Beaufort Gyre dynamics

Spall (2013) proposed that eddy boundary fluxes of buoyancy are balanced by diapycnal diffusion in the gyre interior. In this framework, eddies transport cold, fresh shelf water from the boundary current to the upper halocline and warm, salty Atlantic water to the lower halocline, restoring the stratification that is homogenized by diapycnal diffusion. In this idealized configuration, the ocean was forced with uniform winds and the Ekman convergence is unnecessary to explain the isopycnal profile and boundary currents. As a result, there is an unrealistically homogeneous distribution of the freshwater content in the interior of the Beaufort Gyre and the halocline depth variations are not linked to Ekman pumping as they are in observations (Proshutinsky et al. 2019b).

To explore the role of eddies in the Beaufort Gyre equilibration forced by Ekman pumping, Manucharyan and Spall (2016) and Manucharyan et al. (2016) have developed a single-

layer model using the Transformed Eulerian Mean formalism (Andrews and McIntyre 1976, 1978; Boyd 1976; Vallis 2017). Specifically, Ekman pumping gives rise to a baroclinically unstable tilt of isopycnals, generating mesoscale eddies that reduce their slope via along-isopycnal (i.e., adiabatic) fluxes represented by the Gent–McWilliams (GM) parameterization (Gent and McWilliams 1990). In a steady state, the residual circulation, a sum of the Ekman- and eddy-induced circulations, directly balances buoyancy sources and sinks (Andrews and McIntyre 1976). In the gyre interior, the residual circulation is balanced by diapycnal mixing (an effective volume source/sink of buoyancy) and is thought to be an order of magnitude smaller than the Ekman- and eddy-induced circulations.

Through a phenomenon coined the “ice–ocean stress governor,” Meneghello et al. (2018a) have suggested that the presence of sea ice (i.e., ice–ocean stresses) could obviate the need for an eddy-induced circulation to equilibrate the gyre. In a steady state, the net Ekman pumping might be negligibly small with wind-driven downwelling balancing the ice-driven upwelling—a mechanism also pointed out in Dewey et al. (2018) and Zhong et al. (2018). However, the Beaufort Gyre is not fully ice covered, and observations suggest that the ice–ocean stress governor mechanism reduces the effective strength of the Ekman pumping to about $2\text{--}3\text{ myr}^{-1}$ (Meneghello et al. 2017); this remaining Ekman pumping needs to be counteracted by some process (presumably eddy activity) in order to achieve a steady state. Using a hierarchy of models, Doddridge et al. (2019) have demonstrated that the steady-state balance is determined by wind stress on the ice-free ocean, the ice–ocean governor mechanism, and mesoscale

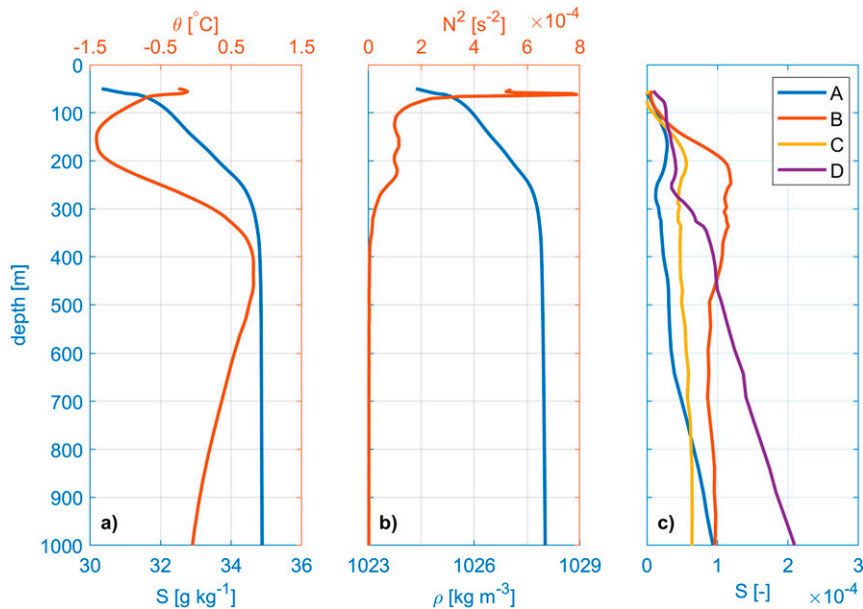


FIG. 2. Time-mean stratification at mooring B: (a) salinity (here labeled “S”; blue) and potential temperature θ (red), (b) potential density ρ (blue) and buoyancy frequency N^2 (red), and (c) mean isopycnal slope S estimated at moorings A–D from the MIMOC.

eddy fluxes. The ice–ocean governor mechanism is thought to dominate the transient evolution on interannual time scales, with eddy fluxes becoming important on longer time scales (Meneghello et al. 2020). Analyzing the interannual gyre variability, Armitage et al. (2020) inferred that the eddy dissipation by friction against the sea ice must be present in order to balance the gyre’s mechanical energy sources and sinks, particularly since 2007 when sea ice concentrations have significantly decreased. Thus, while the ice–ocean governor mechanism does not require eddies, they are nonetheless prominent in the Beaufort Gyre (Zhao et al. 2016, 2018) and their observationally constrained diffusivity can be of sufficient magnitude to counteract the Ekman pumping (Meneghello et al. 2018b) and the accumulation of potential energy (Armitage et al. 2020).

In this study we point out the critical role of eddies in controlling the vertical structure of the Beaufort Gyre halocline. Specifically, we focus on explaining the significant variations of isopycnal slopes with depth that are evident in the climatological state of the gyre (Figs. 1b and 2c). Prior models (e.g., Manucharyan et al. 2016; Doddridge et al. 2019; Meneghello et al. 2020) have represented the halocline as a single layer or as multiple layers with a constant eddy buoyancy diffusivity and cannot explain the vertical structure, as will be demonstrated. To explain the observed isopycnal slope profile, we develop a framework for a multilayer gyre model and use it to evaluate the relative role of Ekman pumping, vertical mixing, and eddy overturning in driving the thickness variability in the PWW layer.

c. Overview of the study

In section 2, we investigate observational data from multiple sources to characterize the mean state and variability of the

isopycnal structure in the Beaufort Gyre, with a focus on the PWW layer. In section 3, we derive a multilayer model that generalizes those of Spall (2013), Manucharyan and Spall (2016), Manucharyan et al. (2016), and Meneghello et al. (2018a) and includes all major physical processes: Ekman pumping, mesoscale eddy activity, and diapycnal diffusion. In the subsequent sections, we quantify how each term in the model contributes to the observed isopycnal slope profile and layer thickness variability in the gyre interior. In section 4, we quantify the depth dependence of the Eulerian-mean vertical velocity and demonstrate that its contribution to the PWW layer thickening is negligible. In section 5, we exclude diapycnal mixing as the cause of the PWW layer thickening. In section 6, we perform modeling experiments to demonstrate that increasing thickness in the gyre interior can be explained by the activity of mesoscale eddies in the GM parameterization if the eddy buoyancy diffusivity coefficient varies with depth. Combining this theoretical framework with observational data, we then infer the vertical structure of the eddy buoyancy diffusivity coefficient. In addition, we discuss the inability of alternative eddy flux parameterizations, such as potential vorticity or thickness diffusion, to explain the layer thickness variability. In section 7, we summarize and discuss the implications of our findings.

2. Observational data

The Ekman pumping velocity in the Canada Basin for 2003–14, including ice–ocean and air–ocean stresses, has been estimated using observations of the surface wind, ocean geostrophic velocity, and sea ice concentration (Meneghello et al. 2017). Annual-mean values of the Ekman pumping velocity

on a 25-km equal-area grid are obtained from the authors and averaged spatially.

The Beaufort Gyre Observing System (BGOS) consists of four moorings (denoted A–D; Fig. 1a), deployed from 2003 to present, which are equipped with McLane Moored Profilers that measure pressure, temperature, salinity, velocity, and other oceanographic variables at high spatial and temporal resolution: two profiles of the ~50–2000-m depth range (staggered by 6 h) are produced every ~54 h. Using the profiles, time series of isopycnal depth and layer thickness are inferred for the PWW (defined by the 1026 and 1027 kg m⁻³ isopycnals). Since our study focuses upon the interannual to decadal variability of the PWW layer thickness, profiles containing high-frequency vertical displacements due to the passage of eddies are removed where possible. For each profile, eddy kinetic energy (EKE) is calculated as

$$\text{EKE} = \frac{1}{2} \int_{z_1}^{z_2} \rho(u^2 + v^2) dz, \quad (1)$$

where ρ is the potential density, u is the zonal velocity, v is the meridional velocity, and $z_1 = -300$ m and $z_2 = -90$ m are the integration bounds (see Zhao et al. 2016). At each mooring (excluding C, where observations are insufficient), isopycnal depth measurements that correspond to EKE exceeding the 90th percentile of available data are removed. Isopycnal depths are then smoothed with a ~90-day moving median filter.

Vertical profiles of the isopycnal slope [$S = -(\partial \bar{b}/\partial r)/(\partial \bar{b}/\partial z)$, where b is the buoyancy] are calculated using the Monthly Isopycnal and Mixed-Layer Ocean Climatology (MIMOC) data (Schmidtko et al. 2013), because the mooring data have insufficient spatial coverage to estimate the radial derivative. The MIMOC product consists of a monthly climatology of salinity and temperature on a $0.5^\circ \times 0.5^\circ$ horizontal grid from 80°S to 90°N and 81 pressure levels from 0 to 1950 dbar. MIMOC ingests a variety of quality-controlled data, primarily from 2007 to 2011, such as Argo floats (Roemmich et al. 2009), Ice-Tethered Profilers (ITPs) (Toole et al. 2011), and the World Ocean Database (Boyer et al. 2009); details of the data processing are provided in Schmidtko et al. (2013). MIMOC has been successfully used to investigate the climatology of the Beaufort Gyre (Meneghello et al. 2017) and is well suited for the present study. At each location, the radial direction is taken to be down the mean horizontal buoyancy gradient in the halocline from 70 to 600 m. The profiles are smoothed to reduce noise.

The stratification of the PWW layer in the “cold halocline” (i.e., the region from ~100 to 200 m in Figs. 2a and 2b; see also Timmermans et al. 2017) is primarily determined by salinity and is characterized by an increase of isopycnal slope with depth in the MIMOC (Fig. 2c). The isopycnals defining the PWW layer generally deepened during 2004–18, suggesting a spinup of the gyre (Figs. 3a–d) while the layer thickness increased (Figs. 3e–h). In section 3, we show that these observations can be explained by the activity of mesoscale eddies in the GM parameterization, where the eddy buoyancy diffusivity coefficient increases with depth. Furthermore, in section 6b, we derive a framework to infer the vertical structure of the eddy

buoyancy diffusivity from the isopycnal depth and thickness variations during the gyre’s transient evolution.

3. Ekman-driven gyre model

a. Model description

The Beaufort Gyre is modeled using the transformed Eulerian mean framework in which the mean buoyancy is advected by the residual circulation, a sum of the Ekman and eddy-induced streamfunctions:

$$\Psi^{\text{res}} = \bar{\Psi} + \Psi^*. \quad (2)$$

Away from continental slopes, the eddy momentum fluxes can be neglected and the Eulerian-mean circulation is given by the Ekman pumping $\bar{\Psi} = \bar{\tau}/(\rho_0 f)$ (Manucharyan and Isachsen 2019), neglecting any vertical variation (shown to be negligible in section 4); here τ is the azimuthal surface stress, ρ_0 is a reference density, and f is the Coriolis parameter. The surface stress $\bar{\tau}$ is composed of the atmosphere–ocean and the ice–ocean components that we do not explicitly separate as we consider the gyre evolution under a general time-dependent stress, $\bar{\tau}(r, t)$.

The eddy-induced overturning represents the cumulative activity of mesoscale eddies that act to reduce the isopycnal slope. Using the GM parameterization (Gent and McWilliams 1990; Gent et al. 1995), the eddy streamfunction Ψ^* is defined by either horizontal or vertical eddy buoyancy fluxes as

$$\Psi^* = -\overline{w'b'}/(\partial \bar{b}/\partial r) = \overline{v'b'}/(\partial \bar{b}/\partial z),$$

where v is the radial velocity, w is the vertical velocity, and primes represent perturbations from the mean. Here horizontal eddy buoyancy fluxes are downgradient; that is,

$$\overline{v'b'} = -K^b \frac{\partial \bar{b}}{\partial r} \quad \text{and} \quad \Psi^* = K^b S, \quad (3)$$

where S is the isopycnal slope and K^b (m² s⁻¹) is the GM eddy buoyancy diffusivity. See section 6a for details of the parameterization.

The Eulerian-mean vertical velocity w^{Ek} and eddy-induced vertical velocity w^* are given by the radial derivatives of the respective streamfunctions. Then the time evolution of the i th isopycnal depth ($h_i > 0$) is controlled by three dynamical processes (Fig. 4): Ekman pumping, mesoscale eddy activity (including boundary fluxes), and diapycnal diffusion. Specifically,

$$\frac{\partial h_i}{\partial t} = \underbrace{\frac{1}{r} \frac{\partial}{\partial r} \left(r \frac{\bar{\tau}}{\rho_0 f} \right)}_{\text{Ekman: } w^{\text{Ek}}} - \underbrace{\frac{1}{r} \frac{\partial}{\partial r} \left(r K_i^b \frac{\partial h_i}{\partial r} \right)}_{\text{eddies: } w^*} - \underbrace{\frac{\partial}{\partial z} \left(\kappa^d \frac{\partial \bar{b}}{\partial z} \right)}_{\text{diabatic: } w^d} \bigg/ \frac{\partial \bar{b}}{\partial z} = 0. \quad (4)$$

An axisymmetric coordinate system is used with r the radial coordinate and z positive up; here $w^{\text{Ek}} < 0$ for Ekman pumping.

The boundary conditions for Eq. (4) have important implications for the gyre dynamics, affecting the equilibration time scale and the mean depth of the halocline. Manucharyan and Spall (2016)

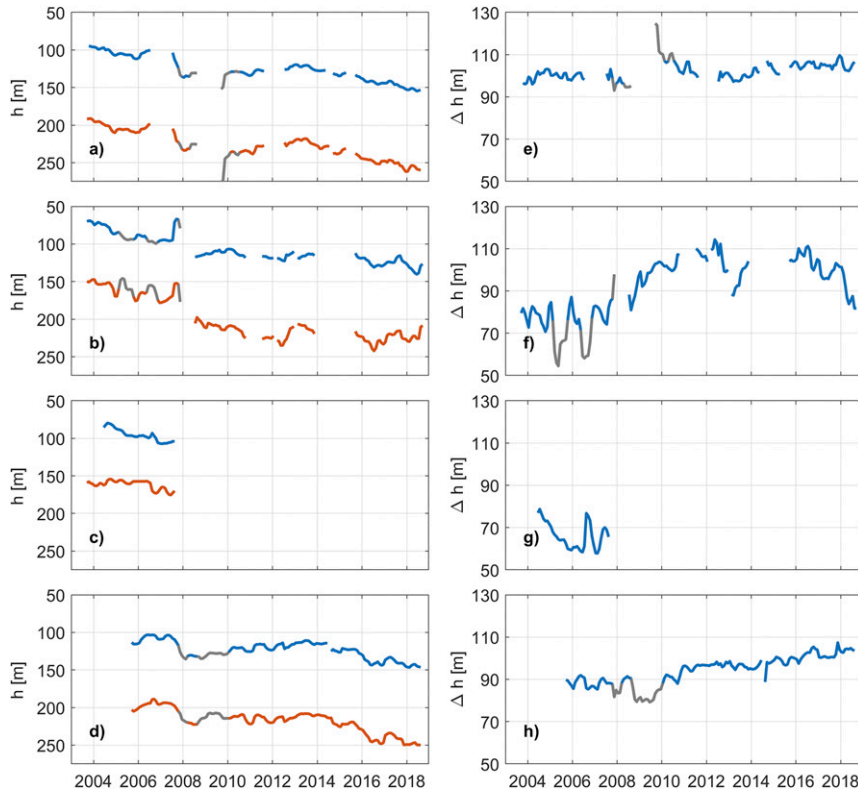


FIG. 3. (left) Depth of the 1026 (blue) and 1027 (red) kg m^{-3} isopycnals corresponding to the upper and lower interfaces of the PWW layer, along with (right) thickness of the PWW layer, i.e., the difference between the two isopycnal interface depths plotted in (a)–(d), at BGOS moorings (a),(e) A; (b),(f) B; (c),(g) C; and (d),(h) D. Isopycnal depths are smoothed with a 90-day moving median filter after removing points with 90–300-m EKE above the 90th percentile. In addition, data shown in gray are manually identified to be outliers of Δh in Δh – h space (see the gray points in Fig. 9, below). This figure is similar to Fig. 5 of Zhong et al. (2019).

and Manucharyan et al. (2016) have chosen a fixed-depth condition:

$$\left. \frac{\partial h_i}{\partial r} \right|_{r=0} = 0, \quad h_i(R) = h_{i0}, \quad (5)$$

where $R \approx 600$ km is the gyre radius. This framework describes a gyre driven by atmospheric forcing; that is, the Ekman-induced velocity (integrated over the gyre interior) drives changes in the isopycnal depth while fluxes through a thin lateral boundary layer dynamically adjust to provide the required volume. There is a limitless availability of water masses of each density class, formed by surface buoyancy fluxes where isopycnals outcrop at the boundary, internal gravity wave breaking, and so on. On the other hand, a boundary flux can be explicitly prescribed:

$$\left. \frac{\partial h_i}{\partial r} \right|_{r=0} = 0, \quad \left. \frac{\partial h_i}{\partial r} \right|_{r=R} = -Q_i / (2\pi R K_i^b), \quad (6)$$

where Q_i ($\text{m}^3 \text{s}^{-1}$) is the volumetric flux outward through the gyre boundary between the surface and the i th isopycnal. Here the flux condition is on the eddy diffusion operator; that is, the

flux is injected to the gyre interior by eddies. In this view, the gyre can be driven by lateral boundary fluxes independent of the Ekman pumping. The choice of $Q_i = 0$ represents a no-flux condition, in which the volume between isopycnals is conserved. Equation (6) implies that the volume flux per unit meter outward through the boundary by eddies is

$$\frac{\partial Q}{\partial z} = 2\pi R \frac{\partial}{\partial z} (K^b S)_{r=R}. \quad (7)$$

Mixed-layer buoyancy fluxes are neglected since only shallow isopycnals in the halocline outcrop away from the boundaries (see, e.g., Fig. 1b) and these fluxes have not been hitherto well constrained.

We separate w^{Ek} into time-dependent and space-dependent components: $w^{\text{Ek}} = p^{\text{Ek}}(t)w_1(r)$, where the prefactor $p^{\text{Ek}}(t)$ is unitless and $w_1(r)$ is an idealized spatial profile. For Eq. (4) with a fixed boundary condition (see discussion of boundary conditions below), we choose a profile of w_1 that is constant in the gyre interior as in Manucharyan and Spall (2016) and Manucharyan et al. (2016) (Fig. 5d). For Eq. (4) with a flux boundary condition, we choose a spatial profile of w_1 corresponding to nearly constant Ekman pumping in the gyre

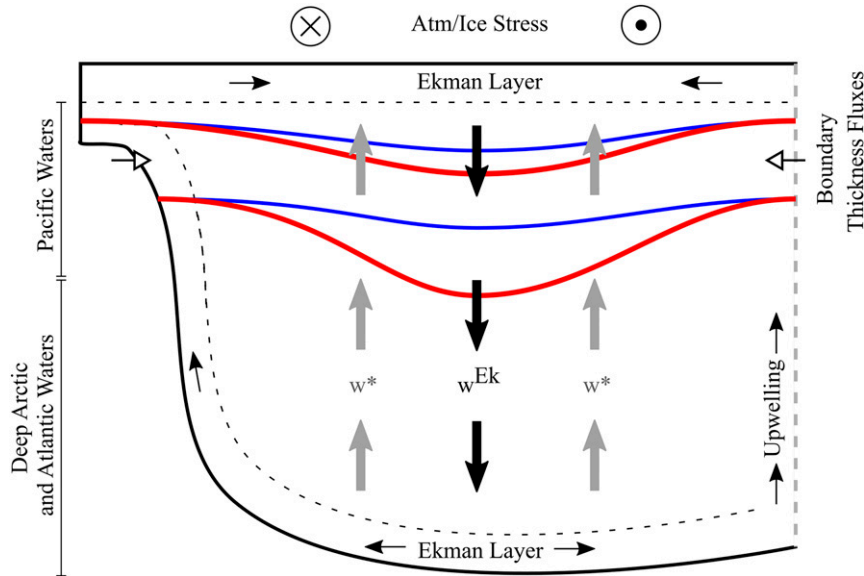


FIG. 4. Schematic of a cross section of the Beaufort Gyre, including the major processes involved in setting its vertical structure. The gyre is bounded by the shelf on the south (left) and is open to the north (right). Eulerian-mean vertical velocity w^{Ek} and eddy-induced vertical velocity w^* are shown. Also shown is an idealized profile of the isopycnals defining the PWW layer in a steady state in which K^b is constant with depth (blue lines) and in a transient state in which the surface stress intensifies and K^b decreases with depth (red lines).

interior, subject to dynamical constraints. Specifically, w_1 has a contribution from strong coastal upwelling near the gyre boundary as suggested by observations and ensures that the model with a flux boundary condition is volume conserving in the absence of boundary fluxes ($Q = 0$) and diapycnal mixing ($w^d = 0$); this is equivalent to the condition $\tau(R) = 0$. Note that Eq. (4) neglects the vertical variation of the Eulerian-mean vertical velocity, which is demonstrated to be small in section 4.

This decomposition of the Ekman pumping is validated by an EOF analysis of the observational data of Meneghello et al. (2017) over the region shown in Figs. 5a–c. The first three EOFs explain about 27%, 21%, and 15% of the variance, respectively. The first and second EOFs contain most of the variance in the radially symmetric patterns, and are qualitatively similar to the idealized spatial patterns of the Ekman pumping (Figs. 5a–d). Last, the velocity induced by diapycnal mixing is parameterized by a diapycnal diffusivity κ^d ($\text{m}^2 \text{s}^{-1}$). For simplicity, we have used the weak-slope approximation and an assumption that the background stratification $\partial \bar{b} / \partial z$ does not substantially change in time or space, resulting in $b - \bar{b} = \partial \bar{b} / \partial z (h - \bar{h})$ for any buoyancy perturbations from the background stratification; the assumption is akin to one commonly used in the quasigeostrophic approximation.

b. Steady-state balance

The profile of the halocline slope contains critical information about the relative contributions of Ekman pumping, mesoscale eddy activity, and diapycnal mixing (Fig. 4) to the dynamical balance. For instance, in a steady state (neglecting diapycnal mixing and the minor variation of Ekman pumping

with depth; see sections 4 and 5), Eq. (4) suggests a formula for the isopycnal slope profile at a distance r from the gyre center:

$$K^b S = -\frac{\bar{\tau}}{\rho_0 f}. \quad (8)$$

Equation (8) implies that, in a steady state, the vertical profile of the isopycnal slope is determined exclusively by the vertical profile of the eddy buoyancy diffusivity. In other words, if K^b is constant, then all isopycnal slopes must be equal and hence all isopycnals are parallel to each other. On the other hand, the observed increase of the mean isopycnal slope with depth in the halocline in the MIMOC (Fig. 2c) suggests that the eddy diffusivity must decrease with depth. Low-resolution ocean models that use a constant eddy diffusivity are unlikely to realistically represent spatial variations of isopycnal thickness in an equilibrated state (or, as we show in section 6c, in a transient state).

If the gyre were fully equilibrated, Eq. (8) would provide a relationship among the (observed) Ekman pumping, isopycnal slope, and (unknown) vertically varying eddy buoyancy diffusivity. Zhong et al. (2019) have used a steady-state argument to estimate the recent isopycnal deepening in the PWW layer due to Ekman pumping and mesoscale eddy activity. Yet during the period 2005–18, the Beaufort Gyre was not in an equilibrated state, and $\partial h / \partial t$ is at least as large as the Ekman- and eddy-induced velocities in Eq. (4) (Figs. 6a,b). Thus, we consider a model for the transient dynamics of the gyre [Eq. (4) with all terms retained; see Fig. 4].

According to this model, several phenomena could potentially account for the expansion of the PWW layer, such as depth variation of Ekman pumping, K^b , diabatic processes, or

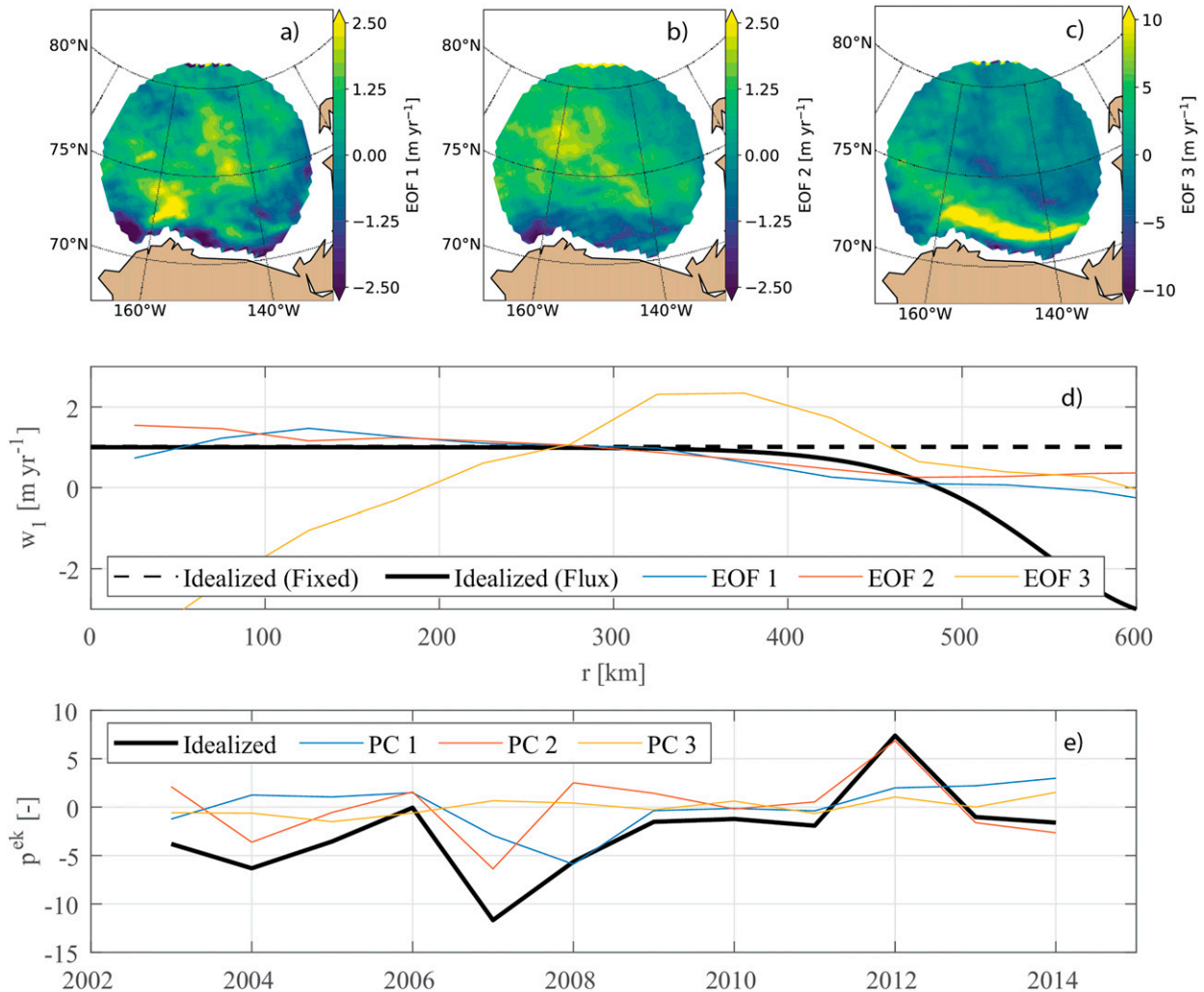


FIG. 5. (a) EOF 1, (b) EOF 2, and (c) EOF 3 of the observed Ekman pumping of Meneghello et al. (2017) over the given region. EOFs are scaled to have mean 1 m yr^{-1} between the gyre center and $\sim 400 \text{ km}$ for comparison with the idealized forcing. (d) Spatial component $w_1(r)$ of the idealized Ekman pumping in the model experiments with the fixed and flux (including no forcing) boundary conditions, and azimuthal mean of the EOFs in (a)–(c). (e) Time-dependent component $p^{Ek}(t)$ of the idealized Ekman pumping velocity in the model experiments and principal components corresponding to the EOFs in (a)–(c). See the text for details.

explicitly prescribed boundary fluxes of buoyancy [i.e., the flux boundary condition of Eq. (6) with $\partial Q/\partial z \neq 0$]. In section 6, we show that thickening of the PWW layer results as a transient response to increasing Ekman pumping in the presence of depth-dependent eddy diffusivity K^b , while the vertical variations of the Ekman pumping velocity (section 4) and diapycnal mixing (section 5) act to contract the layer. In particular, we infer the vertical structure of the eddy buoyancy diffusivity from the transient evolution of the isopycnal depth and layer thickness, and show that, consistent with the structure inferred from Eq. (8), it is decreasing with depth in the PWW layer.

4. Eulerian-mean velocity

In the midlatitudes, where the β effect is nonnegligible, the Sverdrup relation suggests that the Ekman velocity is balanced

by the meridional transport of the water column below the Ekman layer, which leads to a dramatic decay of Ekman pumping velocity with depth [Also, in subtropical gyres, the Ekman-induced vertical velocity has been shown to be opposed by the activity of mesoscale eddies in a model (Doddridge et al. 2016).] Unlike in midlatitude ocean gyres where Sverdrup theory is broadly applicable, the β effect in the Beaufort Gyre is relatively weak. To quantify the vertical variation of the Eulerian-mean velocity in the interior of the Beaufort Gyre, we consider stratified linear dynamics where isopycnals are being displaced by the Ekman pumping velocity and the associated flow is in thermal wind balance.

In this section, we consider all variables to be mean quantities and hence omit the overbars. For simplicity, we assume a Cartesian geometry and a sinusoidal surface stress varying only

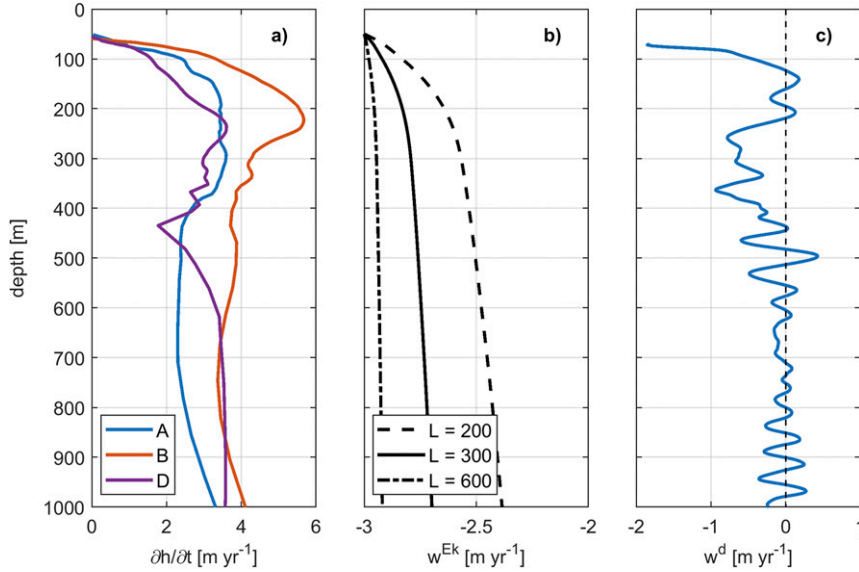


FIG. 6. (a) Estimates of $\partial h/\partial t$, i.e., change of isopycnal depth with time, at indicated BGOS moorings as estimated from the linear trend over the time period of the available data. (b) Ekman pumping velocity penetrating to indicated depth, as calculated from Eq. (12) using the time-mean stratification from BGOS mooring B and the indicated wavelength L (km) of the surface Ekman pumping velocity. (c) Estimates of w^d (i.e., vertical velocity from diapycnal mixing) based on the time-mean $\rho(z)$ at mooring B.

in the y direction is applied to the gyre. Then the vertical Ekman-induced velocity at the base of the Ekman layer assumes the form $w^{\text{Ek}}(y, 0, t) \sim \sin(ky)$, where $k = 2\pi/L$ and L represents a characteristic wavelength. Beneath the Ekman layer, the momentum equations are

$$\frac{\partial u}{\partial t} - fv = -\frac{1}{\rho_0} \frac{\partial p}{\partial x} \quad \text{and} \quad \frac{\partial v}{\partial t} + fu = -\frac{1}{\rho_0} \frac{\partial p}{\partial y}, \quad (9)$$

where (u, v) represent the velocity in the zonal and meridional directions. The flow is assumed to be slowly evolving such that $\partial/\partial t \ll f$. The resulting balance implies that $\partial v/\partial t \ll fu$ and can be neglected. In addition, it is assumed that the flow is hydrostatic, incompressible, and that $N^2 = -(g/\rho_0)(\partial\rho/\partial z)$ varies only vertically. Since w^{Ek} is taken to be independent of x we obtain the following equation set, where p represents the hydrostatic pressure:

$$\frac{\partial p}{\partial z} = -\rho g, \quad \frac{\partial v}{\partial y} + \frac{\partial w^{\text{Ek}}}{\partial z} = 0, \quad \text{and} \quad \frac{\partial \rho}{\partial t} + w^{\text{Ek}} \frac{\partial \rho}{\partial z} = 0. \quad (10)$$

Combining the above equations yields the equation for the Ekman pumping distribution in the interior of the gyre:

$$\frac{\partial^2 w^{\text{Ek}}}{\partial z^2} - \frac{N^2}{f^2} \frac{\partial^2 w^{\text{Ek}}}{\partial y^2} = 0, \quad (11)$$

with the bottom boundary condition taken to be $\partial w^{\text{Ek}}(y, z_b, t)/\partial z = 0$ because $N^2(z_b) \approx 0$, where z_b represents the level of the ocean bottom boundary layer (here assumed to be 4000 m). If w^{Ek} assumes a wave-like ansatz $w^{\text{Ek}} = \Re[\widehat{W}_0(k)e^{iky}\widehat{w}^{\text{Ek}}(z)]$, then the vertically varying component satisfies

$$\frac{\partial^2 \widehat{w}^{\text{Ek}}}{\partial z^2} - \frac{k^2 N^2}{f^2} \widehat{w}^{\text{Ek}} = 0. \quad (12)$$

If the buoyancy frequency N^2 is constant with depth, then Eq. (12) admits an exponentially decaying solution with an e -folding depth of kN/f . However, N^2 is strongly depth dependent in the Beaufort Gyre (Fig. 2b), and therefore we solve Eq. (12) numerically using the observed mean profile of N^2 from mooring B (there is little spatial variability in the stratification between the moorings) and $L = 200, 300,$ and 600 km. (Note that the characteristic length scale of the surface stress in the Beaufort Gyre is uncertain).

The velocity decays by no more than 10% between 100 and 200 m (Fig. 6b) and persists to a bottom boundary layer; for characteristic wavelengths of $L = 200, 300,$ and 600 km, the velocity at 4000 m is $\sim 70\%, 85\%,$ and 95% , respectively, of its value at the base of the surface Ekman layer and hence the bottom Ekman layer is necessary for mass conservation.

Using the ECCO ocean state estimate, Liang et al. (2017) have inferred the vertical structure of the Eulerian vertical velocity and its compensation by the eddy-induced vertical velocity. These estimates also suggest that the Eulerian vertical velocity does not decay significantly within the upper ~ 1000 m of the water column (see their Fig. 1), consistent with our findings. As the magnitude of the vertical Ekman pumping velocity decreases slightly with depth, it cannot be a significant factor in the recent expansion of the PWW layer. Rather, the effect of its vertical variation is a thinning (however negligible) of the layer and for simplicity, Eq. (4) neglects the variation of the Ekman-induced vertical velocity with depth.

5. Diapycnal mixing

The stratification of the PWW layer between ~100 and 200 m is such that diapycnal mixing transiently reduces the layer thickness, even though the long-term effect of diapycnal mixing is to homogenize the water column. This is confirmed by the increase with depth of w^d within the halocline (Fig. 6c).

While observations of diapycnal mixing in the Arctic Ocean vary by several orders of magnitude both spatially and temporally (Rainville and Winsor 2008; Fer 2009; Lique et al. 2014), Lique et al. (2014) have estimated the diapycnal diffusivity at the four BGOS moorings using observations of temperature and velocity from CTDs and acoustic current meters mounted to the moorings. Within the halocline, these estimates generally range from $\sim 10^{-7}$ to $10^{-5} \text{ m}^2 \text{ s}^{-1}$; here we assume a constant $\kappa^d = 10^{-6} \text{ m}^2 \text{ s}^{-1}$. Note that a strongly vertically varying diapycnal eddy diffusivity could potentially change the sign of w^d , but this possibility is beyond the scope of this study.

To further illustrate the contribution of w^d to the layer thickness budget, the mean potential density profile $\rho(z)$ at mooring B is diffused for 5 years by directly solving the diffusion equation

$$\frac{\partial \rho}{\partial t} = \kappa^d \frac{\partial^2 \rho}{\partial z^2} \tag{13}$$

with a no-flux boundary condition. With $\kappa^d = 10^{-6} \text{ m}^2 \text{ s}^{-1}$, the PWW layer contracts by ~2 m over this period.

6. Mesoscale eddies

a. Eddy flux parameterizations

In this section, we investigate the role of mesoscale eddy activity in the transient evolution of the Beaufort Gyre. Eddy flux parameterizations arose from the need for coarse-resolution ocean models to parameterize subgrid-scale baroclinic processes. The optimal parameterization of eddy fluxes is uncertain, and multiple alternatives have been proposed, leading to different dynamics. The development of the GM parameterization around 1990 allowed climate models to run stably without flux corrections for the first time by eliminating the ‘‘Veronis effect’’ (i.e., spurious vertical velocities that result from the then-commonplace horizontal diffusion; see Redi 1982; Gent 2011). The GM scheme is predicated upon the principle that eddy fluxes should extract available potential energy from the fluid by reducing the slope of isopycnals while conserving the volume between isopycnals (Gent et al. 1995). Despite initial comparisons to a diffusion operator, the GM scheme constitutes an along-isopycnal, advective flux of buoyancy by eddy-induced transport velocities (i.e., v^* and w^* ; Gent et al. 1995; Treguier et al. 1997; Abernathey et al. 2013; Griffies 2018). The horizontal eddy velocity satisfies $v^* = \partial(K^b S)/\partial z$, where $S = -\nabla b/(\partial \bar{b}/\partial z)$ represents the slope of buoyancy surfaces. In addition to adiabatic buoyancy fluxes, tracers are diffused along isopycnals with a Redi diffusivity, which differs in general from K^b but is often assumed to be equivalent (Redi 1982; Gent et al. 1995).

Alternatively, mesoscale eddy activity can be represented as a diffusion of potential vorticity within isopycnal layers. In

this case, it follows that $v^* = -K^q \partial S/\partial z$ (neglecting β , the meridional variation of the Coriolis parameter; Gent et al. 1995; Treguier et al. 1997; Abernathey et al. 2013; Griffies 2018). A related variant is the diffusion of thickness between isopycnal interfaces, which is similar to a potential vorticity diffusion. By way of distinction, Treguier et al. (1997) point out that in isopycnal models, the GM parameterization bases eddy fluxes on the height of isopycnals rather than the thickness of isopycnal layers, leading to significant differences in dynamics when the eddy diffusivity coefficient varies vertically.

Observational data suggest that potential vorticity gradients amplified the PWW layer when the gyre circulation intensified, which primarily took place during 2007–10 (e.g., Fig. 8 of Zhong et al. 2019). But if the Ekman-driven Eulerian mean circulation is incapable of affecting the interior PV gradients, what explains the amplification of the interior PV gradients during the gyre spinup and their decrease during spindowns? The effect of diabatic mixing in the gyre interior, away from coastal boundaries and surface mixed layer, is negligibly small on time scales of a few years, implying that answer lies in the eddy dynamics. However, considering the two common eddy parameterizations, the downgradient PV or layer thickness diffusion and the GM parameterization, only one can provide a sensible explanation. A thickness diffusion scheme for the PWW layer would direct eddy thickness fluxes down the mean gradient, i.e., outward from the gyre interior toward the boundary, leading to a reduction in the spatial gradient of thickness. In the absence of diabatic sources of layer thickness at the center of the gyre, the eddies would drive the isopycnals toward a state with zero thickness gradients in which their slopes are parallel. Thus, for a more energetic gyre with presumably stronger eddy variability one would expect to see a reduction of any preexisting interior thickness gradients, in contrast to the observations. The GM eddy parameterization can generate interior thickness gradients even in the absence of a residual mean circulation when the eddy buoyancy diffusivity K^b is depth dependent. Specifically, assuming that K^b is lesser at depth explains not only the observed mean state with nonparallel isopycnals but also the amplification of the interior layer thickness gradients occurring during the gyre spinup.

To illustrate this point, consider an idealized three-layer system described by Eq. (4) and no-flux boundary conditions, neglecting the diapycnal mixing and the depth dependence of the Ekman-induced velocity. Then the thickness (i.e., $H_2 = h_2 - h_1$) evolution equation for the second layer (note that $h_1 = H_1$) is given by

$$\frac{\partial H_2}{\partial t} - \frac{1}{r} \frac{\partial}{\partial r} \left(r K_2^b \frac{\partial H_2}{\partial r} + r \Delta K^b \frac{\partial H_1}{\partial r} \right) = 0, \tag{14}$$

where $K_2^b = K_1^b + \Delta K^b$. When $\Delta K^b = 0$, this equation reduces to a PV diffusion scheme and admits a steady-state solution with parallel isopycnals only. However, when $\Delta K^b \neq 0$, the steady-state solution has isopycnal slopes that vary with depth [i.e., are inversely proportional to the eddy buoyancy diffusivity; see Eq. (8)].

Not only do the GM parameterization and PV diffusion represent different mathematical operators, the corresponding

eddy diffusivity coefficients have different vertical structures in general. By equating the divergence of the eddy-induced fluxes, a relationship between K^q and K^b can be established (Smith and Marshall 2009; Abernathy et al. 2013):

$$K^q \left(\frac{\partial S}{\partial z} - \frac{\beta}{f} \hat{y} \right) = \frac{\partial}{\partial z} (K^b S). \quad (15)$$

Yet, to the authors' knowledge, neither K^b nor K^q has been directly measured in the Beaufort Gyre. Rather, an eddy diffusivity coefficient K^λ that is based on a mixing length framework has been estimated as

$$K^\lambda \sim \lambda U, \quad U = \overline{u'u'}^{1/2}, \quad \lambda = \overline{\theta'\theta'^{1/2}} / |\nabla\theta|, \quad (16)$$

where θ , U , and λ represent the along-isopycnal potential temperature, eddy kinetic energy, and characteristic length scale for the eddy-induced displacement of potential temperature anomalies, respectively; primes represent deviations from a 30-day to 1-yr mean (Meneghello et al. 2017). Thus, K^λ is qualitatively similar to the eddy diffusivity of a passive tracer.

Numerical simulations of the Antarctic Circumpolar Current suggest that eddy diffusivities of different variables can have vastly different vertical structures. In a nonlinear, quasigeostrophic model, K^q was intensified near the critical level (~ 1000 m) at which Rossby waves propagate with the same velocity as the mean flow (Smith and Marshall 2009). In a primitive equation model, the eddy diffusivity of quasigeostrophic potential vorticity, Ertel potential vorticity, and a passive tracer (but not buoyancy) had similar vertical structures below ~ 500 m (Abernathy et al. 2013). While these findings depend upon the location of critical levels (and hence the baroclinic modes) that likely differ between the Beaufort Gyre and the Antarctic Circumpolar Current, they suggest that the equivalence of K^q and K^λ should not be assumed. Therefore, Eq. (15) cannot be directly integrated to obtain K^b , demonstrating the need for alternative methods to infer the vertical structure of the eddy buoyancy diffusivity.

b. Vertical structure of the eddy buoyancy diffusivity: Modeling experiments

To illustrate how the eddy diffusivity profile influences the transient evolution of the gyre, a series of nine numerical experiments are performed (Table 1). Specifically, the gyre model of Eq. (4) is set up with two isopycnal interfaces with initial depths of 100 and 200 m. The model is spun up for 30 years with a constant Ekman pumping velocity of -3 m yr^{-1} and then forced with the interannually varying Ekman pumping of Meneghello et al. (2017). Three idealized profiles of eddy diffusivity are constructed: a uniform profile with $K^b = 400 \text{ m}^2 \text{ s}^{-1}$ for both layers; a profile that is decreasing with depth (K_1^b and $K_2^b = 400$ and $100 \text{ m}^2 \text{ s}^{-1}$ respectively), and a profile that is increasing with depth (K_1^b and $K_2^b = 100$ and $400 \text{ m}^2 \text{ s}^{-1}$ respectively). In addition, the boundary term (fixed boundary, no-flux boundary, and flux boundary) is systematically varied. In the flux case, the approximate PWW volume increase estimated by Zhong et al. (2019) (about $6.7 \times 10^3 \text{ km}^3 \text{ yr}^{-1}$) is forced into the gyre as a specified lateral flux;

TABLE 1. Summary of numerical experiments performed with the three-layer model. Indicated are experiment identifier (ID), upper- and lower-layer eddy buoyancy diffusivity K_1^b and K_2^b ($\text{m}^2 \text{ s}^{-1}$), the data source for Ekman pumping, boundary condition (BC), and length of integration (yr), excluding the spinup period of 30 yr. For forcing, “observed” refers to Ekman pumping that is based on Meneghello et al. (2017) and T^{Ek} refers to the time scale (yr) of the synthetic red noise. For the flux boundary condition, fluxes are estimated from Zhong et al. (2019) (see the text for details).

ID	K_1^b	K_2^b	Forcing	BCs	Duration
1	400	400	Observed	Fixed	12
2	400	400	Observed	No flux	12
3	400	400	Observed	Flux	12
4	400	100	Observed	Fixed	12
5	400	100	Observed	No flux	12
6	400	100	Observed	Flux	12
7	100	400	Observed	Fixed	12
8	100	400	Observed	No flux	12
9	100	400	Observed	Flux	12
10	393	290	$T^{\text{Ek}} = 6$	Fixed	470

there is no injection of volume between the surface and the upper isopycnal. (Note that their estimate is time varying; our results, however, are rather robust to the choice of Q of this order of magnitude.) No boundary forcing is prescribed during the spinup. The vertical variation of the Eulerian-mean velocity and the diapycnal term have been shown to be small and are neglected.

At the end of the spinup period, a steady state has been reached in which the isopycnal slope is inversely proportional to the eddy buoyancy diffusivity, consistent with Eq. (8). In particular, the slope is constant with depth if K^b is constant; see dash-dotted lines in Fig. 7. Next, we discuss the transient dynamics in the experiments with the fixed and no-flux boundary conditions.

When a constant value of the eddy buoyancy diffusivity is imposed, the transient solution is characterized by constant isopycnal layer thickness over time, i.e., all isopycnals evolve in parallel when the model is initialized from a state of parallel isopycnals. (As a consequence of Eq. (4), isopycnals that are not parallel approach a parallel state approximately exponentially if K^b is constant with depth, neglecting the vertical variation of the Ekman pumping and diapycnal mixing.) However, when the eddy diffusivity varies with depth, changes in the Ekman pumping give rise to changes in both the isopycnal depth and layer thickness (cf. Figs. 7a,b and Figs. 7c,d). The relationship between the isopycnal depth and layer thickness variability reflects the eddy buoyancy diffusivity profile. For instance, layer thickness variations in the gyre interior in the experiment with $K_1^b > K_2^b$ are nearly opposite to those of the experiment with $K_2^b > K_1^b$ (Figs. 8e,f). With the fixed boundary condition, Ekman pumping drives changes in both the isopycnal depth and total layer volume if K^b varies with depth, since boundary fluxes depend upon the isopycnal slope at the boundary and hence the eddy diffusivity (Fig. 7b). Even if the total layer volume is constrained to be constant over time (as in the case of the no-flux boundary condition), mesoscale eddy fluxes induce layer thickness changes at fixed

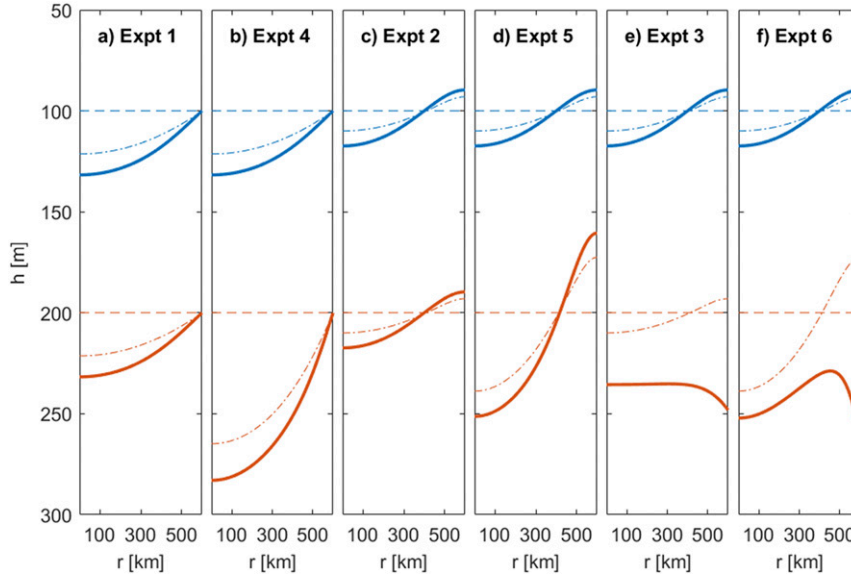


FIG. 7. Various states of the three-layer model from six experiments (summarized in Table 1). Two different profiles of the eddy buoyancy diffusivity are used: uniform profile ($K_1^b = 400 \text{ m}^2 \text{ s}^{-1}$ for both interfaces) and surface-intensified profile ($K_1^b = 400 \text{ m}^2 \text{ s}^{-1}$ and $K_2^b = 100 \text{ m}^2 \text{ s}^{-1}$ for the upper and lower interface, respectively). In addition, three different boundary conditions (fixed, no flux, and flux) are used. The 1026 and 1027 kg m^{-3} isopycnals are represented by the blue and red lines, respectively; the initial state of the model (dashed lines), equilibrated state at the end of the 30-yr spinup (dash-dotted lines), and transient state at a selected time step (solid lines) are given. The experiments shown are (a) uniform eddy diffusivity and fixed boundary condition, (b) surface-intensified eddy diffusivity and fixed boundary condition, (c) uniform eddy diffusivity and no-flux boundary condition, (d) surface-intensified eddy diffusivity and no-flux boundary condition, (e) uniform eddy diffusivity and flux boundary condition, and (f) surface-intensified eddy diffusivity and flux boundary condition.

locations in the gyre interior that are compensated near the boundary (Fig. 7c).

With the flux boundary condition, the isopycnal slope can vary with depth in the transient state even when the eddy buoyancy diffusivity is constant (Fig. 7e). However, this gives rise to a physically unrealistic profile of the isopycnal slope since the isopycnal must be deformed near the boundary to permit a flux into the gyre (Figs. 7e,f). In addition, since the gyre is thought to be driven by Ekman pumping (i.e., lateral fluxes respond to Ekman pumping in the gyre interior) rather than lateral buoyancy fluxes (i.e., boundary fluxes are forced and independent of the interior Ekman pumping), our subsequent theory and discussion focus upon the fixed and no-flux conditions.

c. A diagnostic for the vertical variation of the GM eddy diffusivity coefficient

In this section, we formalize the influence of the eddy diffusivity profile on the isopycnal depth and thickness variability that was observed in the modeling experiments. Considering the steady state solutions of Eq. (8), the difference between the slopes of two isopycnals can be expressed as

$$\frac{\partial}{\partial r}(h_2 - h_1) = \frac{\bar{\tau}}{\rho_0 f} \left(\frac{1}{K_2^b} - \frac{1}{K_1^b} \right). \tag{17}$$

Replacing radial derivatives by Δr according to a scaling relation, Eq. (17) implies a relationship between the characteristic isopycnal thickness, isopycnal depth variations, and the ratio of eddy diffusivities:

$$\frac{h_2 - h_1}{h_1} = \frac{K_1^b}{K_2^b} - 1. \tag{18}$$

This equation, combined with the variability of PWW isopycnal layer depths and thicknesses (Fig. 3) from the mooring observations, suggests the approximate profile of the eddy buoyancy diffusivity. The slope of the linear regression of Δh and h (Fig. 9) is an estimate of the left-hand side of Eq. (18). Using the observational data, the regression suggests that the eddy buoyancy diffusivity is $\sim 10\%$, 40% , and 30% greater at the upper interface than the lower interface of the PWW layer for moorings A, B, and D, respectively. In this estimate, apparent outlying data points (gray dots in Fig. 3) are removed. If all the data were included, the estimates would change to $\sim 10\%$, 50% , and 20% , respectively. As will be subsequently quantified, these values likely underestimate the true ratio.

Equation (18) assumes that the gyre evolves in a state of dynamical equilibrium, which would be approximately satisfied if the temporal variation of Ekman pumping were at a lower frequency than the eddy-driven gyre equilibration time scale. The presence of Ekman pumping variability at a higher

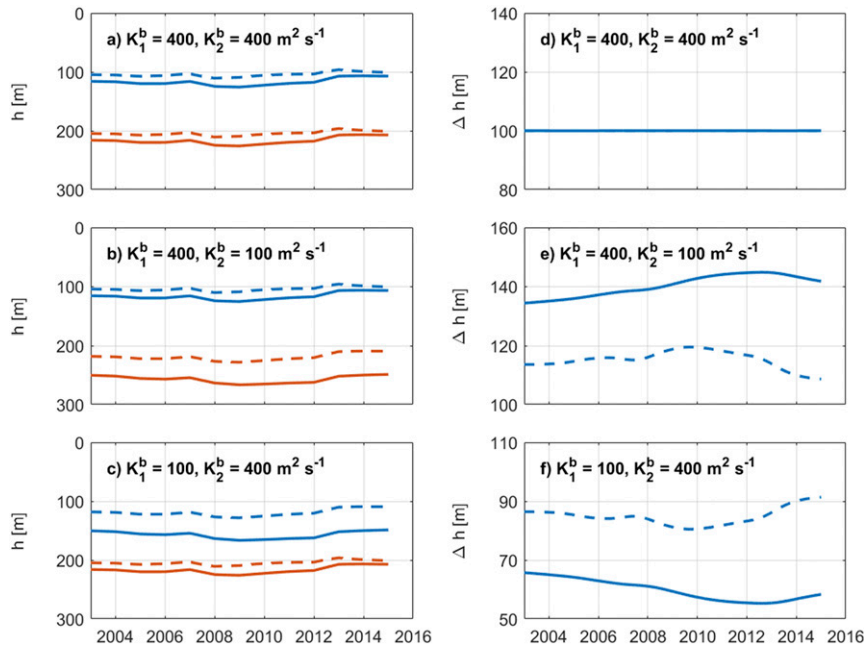


FIG. 8. Time series of (a)–(c) depth h of the 1026 (blue) and 1027 kg m⁻³ (red) isopycnals, and (d)–(f) thickness Δh between the isopycnals, from selected model experiments (summarized in Table 1), forced with the observed Ekman pumping of Fig. 5e, with indicated profiles of the eddy buoyancy diffusivity, at a spatial location about 300 km from the gyre center. Dash patterns indicate different boundary conditions: fixed (solid line) and no flux (dashed line).

frequency than the gyre equilibration time scale would potentially introduce noise into Eq. (18). While the Ekman pumping and gyre equilibration time scales are not fully constrained by observations, several estimates of relevant time scales do exist. Experiments with a barotropic ocean–sea ice

model forced with observed atmospheric variables suggest that the ocean circulation alternates between anomalously anticyclonic and cyclonic regimes with a 10–14-yr period (Proshutinsky and Johnson 1997; Proshutinsky et al. 2002, 2015), suggesting that the atmospheric forcing has an interannual to

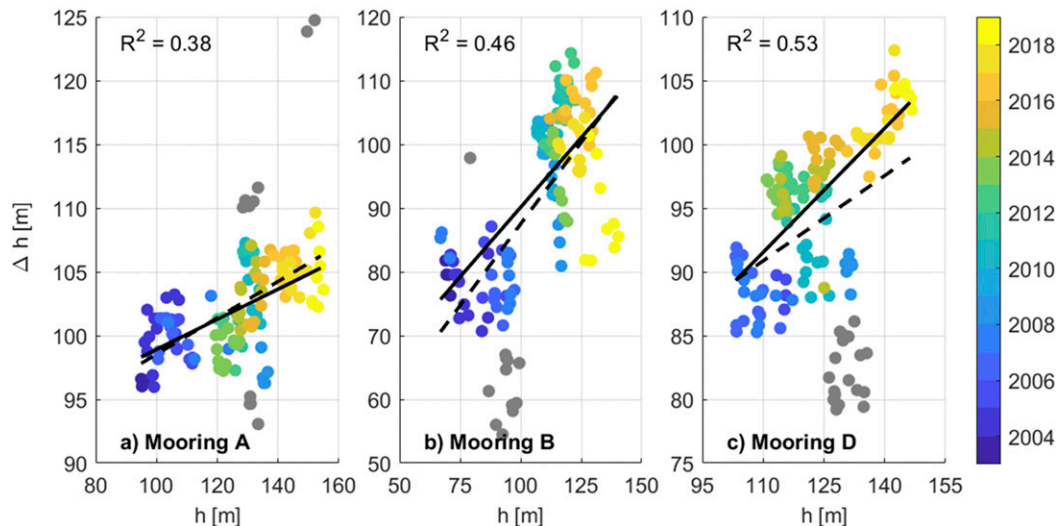


FIG. 9. Scatterplot of Δh for the two isopycnals bounding the PWW layer (1026 and 1027 kg m⁻³) and h (for the upper isopycnal); the same data are plotted as a time series in Fig. 3. A linear least squares fit over all data (dashed black line) and with apparent outliers of Δh (gray points) manually identified and removed (solid black line) is given; the slope is an estimate of the left-hand side of Eq. (18). The coefficient of determination R^2 is given in the upper left of each panel.

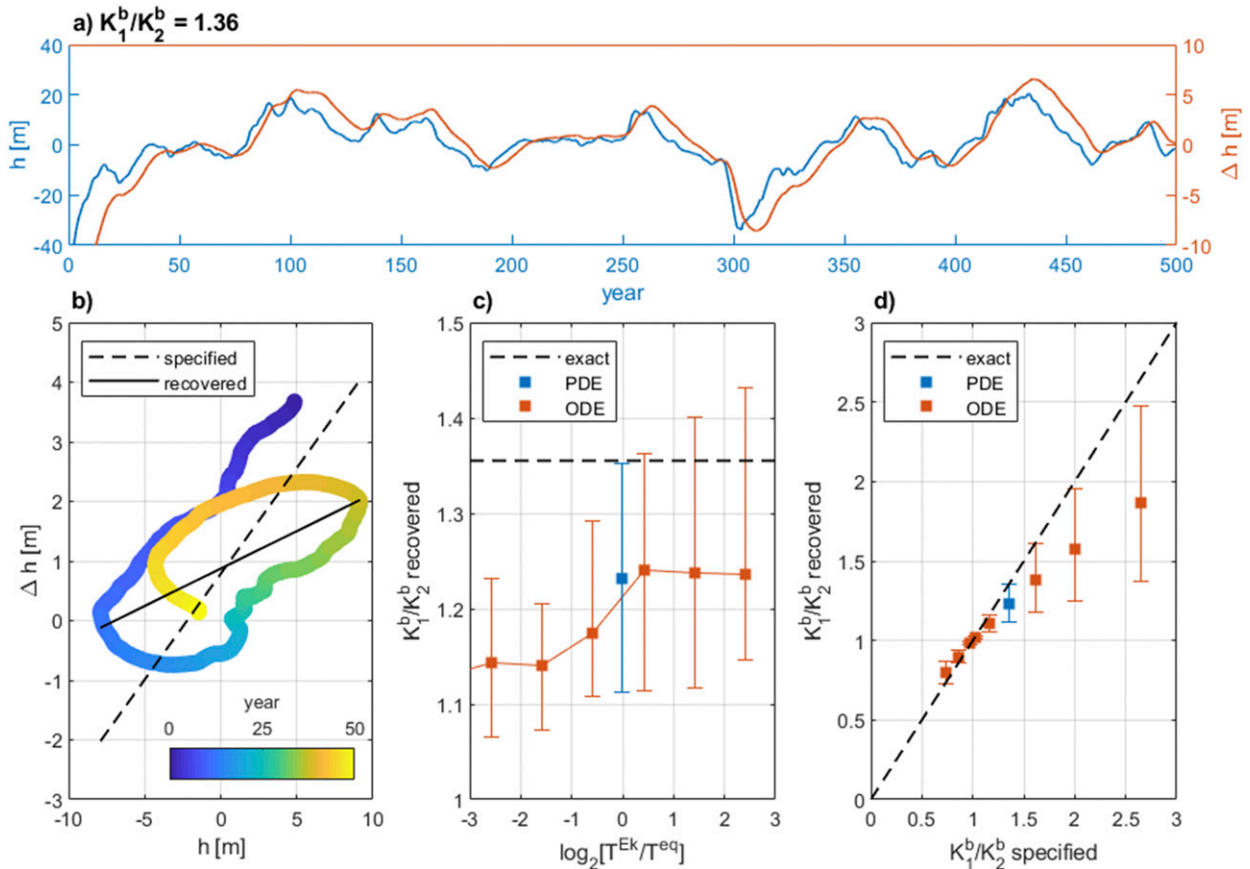


FIG. 10. (a) Time series of h (blue) and Δh (anomalies from time mean; red) from experiment 10 (see Table 1). (b) Scatterplot of Δh vs h from experiment 10 about 300 km from the gyre center to the boundary during a selected 50-yr period. The slope of the dashed black line represents the left-hand side of Eq. (18); the slope of the solid black line represents that recovered from least squares fit to modeled data. (c) Scatterplot of K_1^b/K_2^b vs $T^{\text{Ek}}/T^{\text{eq}}$ from a regression of Δh and h . ODE data are from Eq. (19); PDE refers to experiment 10. The dashed line represents the specified ratio. (d) Scatterplot of recovered vs specified K_1^b/K_2^b for $T^{\text{Ek}} \approx T^{\text{eq}} \approx 6$ yr. Deviation from the dashed line represents the error. In (c) and (d), boxes represent the mean of the distribution of regression coefficients over 50-yr moving windows of the data; error bars are the 5th and 95th percentiles.

decadal memory. It was also shown that the Beaufort Gyre freshwater content has a decadal memory of the sea level pressure field (Johnson et al. 2018). The equilibration time scale of ~ 5 years was estimated for a surface stress-driven gyre and shown to be inversely proportional to the mesoscale eddy diffusivity (Manucharyan and Spall 2016). In addition, numerical simulations reveal that the eddy field itself might require a significant equilibration time scale of 2–6 years because of the so-called eddy memory effect (Manucharyan et al. 2017).

To investigate how the estimates of K^b depend on the time scale of the Ekman pumping variability, we perform numerical experiments with various synthetic forcing, each constructed as a red noise process with a specified persistence time scale T^{Ek} . These time series are scaled to produce reasonable means and variances compared with observations. We integrate the three-layer model with $T^{\text{Ek}} \approx T^{\text{eq}} \approx 6$ yr (where T^{eq} is the mean of the two interfaces) for 500 years, treating the initial 30-yr period as a spinup (experiment 10; Fig. 10a). A distribution of K_1^b/K_2^b is obtained by regressing Δh and h over all overlapping

moving windows of length 50 years (for downsampled data; the spinup is excluded). Means and 90% confidence intervals are then constructed from the resulting distributions. An illustration of the method of estimating K_1^b/K_2^b is presented in Figs. 10a and 10b.

Next, we consider a simplified model of the isopycnal depth to reduce computational complexity. Manucharyan et al. (2016) investigated the adjustment time scale and the general freshwater content response to Ekman pumping variability in a single-layer model and found that they follow the evolution of the least damped halocline eigenmode, conforming to a forced exponential decay equation. Similarly, we model isopycnal thickness perturbations h_i for two interfaces $i = \{1, 2\}$ as

$$\frac{dh_i}{dt} = -\frac{h_i}{T_i^{\text{eq}}} + w^{\text{Ek}}, \quad (19)$$

where the e -folding decay time scale is inversely proportional to the eddy diffusivity; that is, $T^{\text{eq}} = cR^2/K^b$, with $c \approx 1/5.7$. The ordinary differential equation (ODE) is integrated for 500 years,

forced with Ekman pumping represented by the red noise processes with various T^{Ek} . Distributions of K_1^b/K_2^b are constructed, and confidence intervals are constructed using the same method as for the partial differential equation (PDE); see Figs. 10c and 10d.

The error in recovering the ratio of eddy diffusivities from Eq. (18) generally decreases as T^{Ek} increases above T^{eq} (Fig. 10c) and the method tends to underestimate K_1^b/K_2^b when $K_1^b > K_2^b$. Similarly, the method tends to overestimate K_1^b/K_2^b when $K_1^b < K_2^b$. The underestimation is scale dependent, such that as the magnitude of K_1^b/K_2^b increases, the bias increases (Fig. 10d). (As the deviation of K^b between the two layers increases, the deviation of the eddy equilibration time scale also increases, such that variations in layer depth evolve less coherently with variations in layer thickness.) For representative choices of K^b and $T^{\text{Ek}} \approx T^{\text{eq}} \approx 6$ yr (experiment 10), the method recovers a ratio of K_1^b/K_2^b that is about 90% of that specified (Fig. 10d). Thus, Eq. (18) provides a reasonable estimate of the eddy buoyancy diffusivity ratio.

7. Summary and discussion

Observations suggest that the slope of isopycnals in the Beaufort Gyre halocline increases with depth (Fig. 2c). Furthermore, during 2004–18, the isopycnals defining the PWW water mass deepened, while the layer increased in volume (Fig. 3; Zhong et al. 2019). Yet the baroclinic structure of the gyre and the recent expansion of the PWW layer cannot be adequately explained by existing theories that treat the halocline as a single layer.

In this study, we have developed a multilayer gyre model that incorporates all relevant dynamics: Ekman pumping, mesoscale eddy activity, and diapycnal mixing. We demonstrated that in the mean state, the increase of isopycnal slope with depth in the PWW layer can be attributable to the eddy-induced streamfunction, but only if the eddy buoyancy diffusivity decreases with depth. We provided further support for this statement by considering the transient gyre evolution, since the volume of PWW has been significantly changing during recent decades. Specifically, we combined the model framework with observational data to diagnose the contribution of key processes to the transient state of the gyre. The Eulerian-mean velocity and diapycnal mixing act to contract, rather than expand, the PWW layer, although these effects are relatively minor. Only the eddy overturning streamfunction can account for the PWW layer expansion, and this similarly requires that the eddy buoyancy diffusivity decrease with depth. Using a scaling law and the observed temporal variability of the isopycnal depth and layer thickness, we infer that depending on the mooring location, the eddy buoyancy diffusivity decreases by ~10%–40% over the PWW layer.

Our results attest to crucial differences in dynamics between the GM parameterization and thickness diffusion: mesoscale eddy activity can create, rather than homogenize, thickness gradients in the GM parameterization if the eddy buoyancy diffusivity varies vertically. The observed vertical structure and evolution of the Beaufort Gyre halocline can

thus be explained when eddy fluxes are represented by the GM parameterization, but not the thickness diffusion scheme. Thus, the use of a depth-independent GM eddy diffusivity, as is commonly found in low-resolution ocean models, could lead to misrepresentation of the gyre dynamics and an inadequate flux of PWW into the deep basin. However, constraining the true vertical profile of the eddy diffusivity from mooring observations is challenging, and simply using the mixing length relation based on along-isopycnal temperature fluctuations could provide misleading estimates since the diffusivities of buoyancy, potential vorticity, and a passive tracer can have very different vertical structures in general. Given the importance of the vertical structure of the eddy buoyancy diffusivity to the transient and equilibrated gyre dynamics, it is crucial to provide constraints by observing the Beaufort Gyre not only at large-scale but also at eddy scales.

The conclusions of our study rely on a set of simplifying idealizations of otherwise complex gyre dynamics. For instance, we have assumed an axisymmetric gyre with uniform radial boundary fluxes, yet it is possible that a volume could be fluxed into the gyre in one location and fluxed out, in whole or part, elsewhere. Another possibility is that our model neglects some as-yet-unquantified buoyancy source in the interior of the PWW layer, such as convective plumes associated with sea ice formation/brine rejection. In addition, our calculation of the Eulerian mean overturning is idealized as it considers only large-scale balances to arrive at the relation that $\bar{\Psi} = \bar{\tau}/(\rho_0 f)$, yet it is plausible that, with a complex coastal geometry, the eddy momentum fluxes (particularly at the continental slopes, but also within the deep basin) that were omitted could lead to substantial modifications to the Eulerian mean streamfunction (Manucharyan and Isachsen 2019). Whether any of these omitted processes can significantly affect our formed understanding of the role of eddies in shaping the vertical structure of the halocline remains to be explored.

Acknowledgments. The authors acknowledge the GFD Summer Program held at Woods Hole Oceanographic Institution (WHOI) where part of the work was undertaken as well as stimulating discussions at the 2018 FAMOS meeting. In particular, we thank Sam Pegler, Joe Pedlosky, Jack Whitehead, Mary-Louise Timmermans, Glenn Flierl, and others. Author Kenigson received partial support from NSF OCE Grant 1558736 and the Yale Institute for Biospheric Studies (YIBS) Donnelley Fellowship. Author Gelderloos acknowledges funding from NOAA Grant NA15OAR4310172. Author Manucharyan acknowledges support from the NSF OCE Grant 1829969. We also thank the authors of Meneghello et al. (2017) for providing their published estimates of the Ekman pumping and K^A . In addition, we thank Ed Doddridge and an anonymous reviewer for helpful suggestions that improved the paper.

Data availability statement. The MIMOC is available online (<https://www.pmel.noaa.gov/mimoc/>). The BGOS mooring data are available from WHOI (<https://www.whoi.edu/>). The TEOS-10 toolbox (IOC et al. 2010) was used convert among oceanographic variables.

REFERENCES

- Abernathy, R., D. Ferreira, and A. Klocker, 2013: Diagnostics of isopycnal mixing in a circumpolar channel. *Ocean Modell.*, **72**, 1–16, <https://doi.org/10.1016/j.ocemod.2013.07.004>.
- Andrews, D. G., and M. E. McIntyre, 1976: Planetary waves in horizontal and vertical shear: The generalized Eliassen–Palm relation and the mean zonal acceleration. *J. Atmos. Sci.*, **33**, 2031–2048, [https://doi.org/10.1175/1520-0469\(1976\)033<2031:PWIHAV>2.0.CO;2](https://doi.org/10.1175/1520-0469(1976)033<2031:PWIHAV>2.0.CO;2).
- , and —, 1978: Generalized Eliassen–Palm and Charney–Drazin theorems for waves on axisymmetric mean flows in compressible atmospheres. *J. Atmos. Sci.*, **35**, 175–185, [https://doi.org/10.1175/1520-0469\(1978\)035<0175:GEPACD>2.0.CO;2](https://doi.org/10.1175/1520-0469(1978)035<0175:GEPACD>2.0.CO;2).
- Armitage, T. W., G. E. Manucharyan, A. A. Petty, R. Kwok, and A. F. Thompson, 2020: Enhanced eddy activity in the Beaufort Gyre in response to sea ice loss. *Nat. Commun.*, **11**, 761, <https://doi.org/10.1038/s41467-020-14449-z>.
- Belkin, I. M., 2004: Propagation of the “Great Salinity Anomaly” of the 1990s around the northern North Atlantic. *Geophys. Res. Lett.*, **31**, L08306, <https://doi.org/10.1029/2003GL019334>.
- , S. Levitus, J. Antonov, and S.-A. Malmberg, 1998: “Great Salinity Anomalies” in the North Atlantic. *Prog. Oceanogr.*, **41**, 1–68, [https://doi.org/10.1016/S0079-6611\(98\)00015-9](https://doi.org/10.1016/S0079-6611(98)00015-9).
- Boyd, J. P., 1976: The noninteraction of waves with the zonally averaged flow on a spherical Earth and the interrelationships on eddy fluxes of energy, heat and momentum. *J. Atmos. Sci.*, **33**, 2285–2291, [https://doi.org/10.1175/1520-0469\(1976\)033<2285:TNOWWT>2.0.CO;2](https://doi.org/10.1175/1520-0469(1976)033<2285:TNOWWT>2.0.CO;2).
- Boyer, T. P., and Coauthors, 2009: World Ocean Database 2009. NOAA Atlas NESDIS 66, 216 pp., http://www.nodc.noaa.gov/OCS/WOD09/pr_wod09.html.
- Buckley, M. W., and J. Marshall, 2016: Observations, inferences, and mechanisms of the Atlantic meridional overturning circulation: A review. *Rev. Geophys.*, **54**, 5–63, <https://doi.org/10.1002/2015RG000493>.
- Dewey, S., J. Morison, R. Kwok, S. Dickinson, D. Morison, and R. Andersen, 2018: Arctic ice-ocean coupling and gyre equilibration observed with remote sensing. *Geophys. Res. Lett.*, **45**, 1499–1508, <https://doi.org/10.1002/2017GL076229>.
- Dickson, R. R., J. Meincke, S.-A. Malmberg, and A. J. Lee, 1988: The “great salinity anomaly” in the northern North Atlantic 1968–1982. *Prog. Oceanogr.*, **20**, 103–151, [https://doi.org/10.1016/0079-6611\(88\)90049-3](https://doi.org/10.1016/0079-6611(88)90049-3).
- Doddridge, E. W., D. P. Marshall, and A. M. Hogg, 2016: Eddy cancellation of the Ekman cell in subtropical gyres. *J. Phys. Oceanogr.*, **46**, 2995–3010, <https://doi.org/10.1175/JPO-D-16-0097.1>.
- , G. Meneghello, J. Marshall, J. Scott, and C. Lique, 2019: A three-way balance in the Beaufort Gyre: The ice-ocean governor, wind stress, and eddy diffusivity. *J. Geophys. Res. Oceans*, **124**, 3107–3124, <https://doi.org/10.1029/2018JC014897>.
- Fer, I., 2009: Weak vertical diffusion allows maintenance of cold halocline in the central Arctic. *Atmos. Ocean. Sci. Lett.*, **2**, 148–152, <https://doi.org/10.1080/16742834.2009.11446789>.
- Gelderloos, R., F. Straneo, and C. A. Katsman, 2012: Mechanisms behind the temporary shutdown of deep convection in the Labrador Sea: Lessons from the great salinity anomaly years 1968–71. *J. Climate*, **25**, 6743–6755, <https://doi.org/10.1175/JCLI-D-11-00549.1>.
- Gent, P. R., 2011: The Gent–McWilliams parameterization: 20/20 hindsight. *Ocean Modell.*, **39**, 2–9, <https://doi.org/10.1016/j.ocemod.2010.08.002>.
- , and J. C. McWilliams, 1990: Isopycnal mixing in ocean circulation models. *J. Phys. Oceanogr.*, **20**, 150–155, [https://doi.org/10.1175/1520-0485\(1990\)020<0150:MIIOCML>2.0.CO;2](https://doi.org/10.1175/1520-0485(1990)020<0150:MIIOCML>2.0.CO;2).
- , J. Willebrand, T. J. McDougall, and J. C. McWilliams, 1995: Parameterizing eddy-induced tracer transports in ocean circulation models. *J. Phys. Oceanogr.*, **25**, 463–474, [https://doi.org/10.1175/1520-0485\(1995\)025<0463:PEITTI>2.0.CO;2](https://doi.org/10.1175/1520-0485(1995)025<0463:PEITTI>2.0.CO;2).
- Griffies, S., 2018: *Fundamentals of Ocean Climate Models*. Princeton University Press, 528 pp.
- Haine, T. W. N., and Coauthors, 2015: Arctic freshwater export: Status, mechanisms, and prospects. *Global Planet. Change*, **125**, 13–35, <https://doi.org/10.1016/j.gloplacha.2014.11.013>.
- IOC, SCOR, and IAPSO, 2010: The international thermodynamic equation of seawater – 2010: Calculation and use of thermodynamic properties. UNESCO Intergovernmental Oceanographic Commission, Manuals and Guides 56, 196 pp., http://www.teos-10.org/pubs/TEOS-10_Manual.pdf.
- Jackson, L., and M. Vellinga, 2013: Multidecadal to centennial variability of the AMOC: HadCM3 and a perturbed physics ensemble. *J. Climate*, **26**, 2390–2407, <https://doi.org/10.1175/JCLI-D-11-00601.1>.
- Johnson, H. L., S. B. Cornish, Y. Kostov, E. Beer, and C. Lique, 2018: Arctic Ocean freshwater content and its decadal memory of sea-level pressure. *Geophys. Res. Lett.*, **45**, 4991–5001, <https://doi.org/10.1029/2017GL076870>.
- Lauvset, S. K., A. Brakstad, K. Våge, A. Olsen, E. Jeansson, and K. A. Mork, 2018: Continued warming, salinification and oxygenation of the Greenland Sea gyre. *Tellus*, **70A**, 1–9, <https://doi.org/10.1080/16000870.2018.1476434>.
- Liang, X., M. Spall, and C. Wunsch, 2017: Global ocean vertical velocity from a dynamically consistent ocean state estimate. *J. Geophys. Res. Oceans*, **122**, 8208–8224, <https://doi.org/10.1002/2017JC012985>.
- Lique, C., J. D. Guthrie, M. Steele, A. Proshutinsky, J. H. Morison, and R. Krishfield, 2014: Diffusive vertical heat flux in the Canada Basin of the Arctic Ocean inferred from moored instruments. *J. Geophys. Res. Oceans*, **119**, 496–508, <https://doi.org/10.1002/2013JC009346>.
- Manucharyan, G. E., and M. A. Spall, 2016: Wind-driven freshwater buildup and release in the Beaufort Gyre constrained by mesoscale eddies. *Geophys. Res. Lett.*, **43**, 273–282, <https://doi.org/10.1002/2015GL065957>.
- , and P. E. Isachsen, 2019: Critical role of continental slopes in halocline and eddy dynamics of the Ekman-driven Beaufort Gyre. *J. Geophys. Res. Oceans*, **124**, 2679–2696, <https://doi.org/10.1029/2018JC014624>.
- , M. A. Spall, and A. F. Thompson, 2016: A theory of the wind-driven Beaufort Gyre variability. *J. Phys. Oceanogr.*, **46**, 3263–3278, <https://doi.org/10.1175/JPO-D-16-0091.1>.
- , A. F. Thompson, and M. A. Spall, 2017: Eddy memory mode of multidecadal variability in residual-mean ocean circulations with application to the beaufort gyre. *J. Phys. Oceanogr.*, **47**, 855–866, <https://doi.org/10.1175/JPO-D-16-0194.1>.
- Meneghello, G., J. Marshall, S. T. Cole, and M.-L. Timmermans, 2017: Observational inferences of lateral eddy diffusivity in the halocline of the Beaufort Gyre. *Geophys. Res. Lett.*, **44**, 12 331–12 338, <https://doi.org/10.1002/2017GL075126>.
- , —, J.-M. Campin, E. Doddridge, and M.-L. Timmermans, 2018a: The ice-ocean governor: Ice-ocean stress feedback limits Beaufort Gyre spin-up. *Geophys. Res. Lett.*, **45**, 11–293, <https://doi.org/10.1029/2018GL080171>.
- , —, M.-L. Timmermans, and J. Scott, 2018b: Observations of seasonal upwelling and downwelling in the beaufort sea

- mediated by sea ice. *J. Phys. Oceanogr.*, **48**, 795–805, <https://doi.org/10.1175/JPO-D-17-0188.1>.
- , E. Doddridge, J. Marshall, J. Scott, and J.-M. Campin, 2020: Exploring the role of the “ice–ocean governor” and mesoscale eddies in the equilibration of the Beaufort Gyre: Lessons from observations. *J. Phys. Oceanogr.*, **50**, 269–277, <https://doi.org/10.1175/JPO-D-18-0223.1>.
- Proshutinsky, A., R. H. Bourke, and F. A. McLaughlin, 2002: The role of the Beaufort Gyre in Arctic climate variability: Seasonal to decadal climate scales. *Geophys. Res. Lett.*, **29**, 2100, <https://doi.org/10.1029/2002GL015847>.
- , D. Dukhovskoy, M.-L. Timmermans, R. Krishfield, and J. L. Bamber, 2015: Arctic circulation regimes. *Philos. Trans. Roy. Soc.*, **373A**, 20140160, <https://doi.org/10.1098/rsta.2014.0160>.
- , and Coauthors, 2019: Analysis of the Beaufort Gyre freshwater content in 2003–2018. *J. Geophys. Res. Oceans*, **124**, 9658–9689, <https://doi.org/10.1029/2019JC015281>.
- , R. Krishfield, and M.-L. Timmermans, 2020: Introduction to special collection on Arctic Ocean Modeling and Observational Synthesis (FAMOS) 2: Beaufort Gyre phenomenon. *J. Geophys. Res. Oceans*, **125**, e2019JC015400, <https://doi.org/10.1029/2019JC015400>.
- Proshutinsky, A. Y., and M. A. Johnson, 1997: Two circulation regimes of the wind-driven Arctic Ocean. *J. Geophys. Res.*, **102**, 12 493–12 514, <https://doi.org/10.1029/97JC00738>.
- Rainville, L., and P. Winsor, 2008: Mixing across the Arctic Ocean: Microstructure observations during the Beringia 2005 expedition. *Geophys. Res. Lett.*, **35**, L08606, <https://doi.org/10.1029/2008GL033532>.
- Redi, M. H., 1982: Oceanic isopycnal mixing by coordinate rotation. *J. Phys. Oceanogr.*, **12**, 1154–1158, [https://doi.org/10.1175/1520-0485\(1982\)012<1154:OIMBCR>2.0.CO;2](https://doi.org/10.1175/1520-0485(1982)012<1154:OIMBCR>2.0.CO;2).
- Roemmich, D., and Coauthors, 2009: The Argo Program: Observing the global ocean with profiling floats. *Oceanography*, **22**, 34–43, <https://doi.org/10.5670/oceanog.2009.36>.
- Schmidtko, S., G. C. Johnson, and J. M. Lyman, 2013: MIMOC: A global monthly isopycnal upper-ocean climatology with mixed layers. *J. Geophys. Res. Oceans*, **118**, 1658–1672, <https://doi.org/10.1002/jgrc.20122>.
- Smith, K. S., and J. Marshall, 2009: Evidence for enhanced eddy mixing at middepth in the Southern Ocean. *J. Phys. Oceanogr.*, **39**, 50–69, <https://doi.org/10.1175/2008JPO3880.1>.
- Spall, M. A., 2013: On the circulation of Atlantic Water in the Arctic Ocean. *J. Phys. Oceanogr.*, **43**, 2352–2371, <https://doi.org/10.1175/JPO-D-13-079.1>.
- Timmermans, M.-L., J. Marshall, A. Proshutinsky, and J. Scott, 2017: Seasonally derived components of the Canada Basin halocline. *Geophys. Res. Lett.*, **44**, 5008–5015, <https://doi.org/10.1002/2017GL073042>.
- Toole, J. M., R. A. Krishfield, M.-L. Timmermans, and A. Proshutinsky, 2011: The ice-tethered profiler: Argo of the Arctic. *Oceanography*, **24**, 126–135, <https://doi.org/10.5670/oceanog.2011.64>.
- Treguier, A.-M. I. Held, and V. Larichev, 1997: Parameterization of quasigeostrophic eddies in primitive equation ocean models. *J. Phys. Oceanogr.*, **27**, 567–580, [https://doi.org/10.1175/1520-0485\(1997\)027<0567:POQEIP>2.0.CO;2](https://doi.org/10.1175/1520-0485(1997)027<0567:POQEIP>2.0.CO;2).
- Vallis, G. K., 2017: *Atmospheric and Oceanic Fluid Dynamics*. 2nd ed. Cambridge University Press, 964pp.
- Zhao, M., M.-L. Timmermans, S. Cole, R. Krishfield, and J. Toole, 2016: Evolution of the eddy field in the Arctic Ocean’s Canada Basin, 2005–2015. *Geophys. Res. Lett.*, **43**, 8106–8114, <https://doi.org/10.1002/2016GL069671>.
- , —, R. Krishfield, and G. Manucharyan, 2018: Partitioning of kinetic energy in the Arctic Ocean’s Beaufort Gyre. *J. Geophys. Res. Oceans*, **123**, 4806–4819, <https://doi.org/10.1029/2018JC014037>.
- Zhong, W., M. Steele, J. Zhang, and J. Zhao, 2018: Greater role of geostrophic currents in Ekman dynamics in the western Arctic Ocean as a mechanism for Beaufort gyre stabilization. *J. Geophys. Res. Oceans*, **123**, 149–165, <https://doi.org/10.1002/2017JC013282>.
- , —, —, and S. T. Cole, 2019: Circulation of Pacific winter water in the western Arctic Ocean. *J. Geophys. Res. Oceans*, **124**, 863–881, <https://doi.org/10.1029/2018JC014604>.